Journal of Wind Engineering & Industrial Aerodynamics 217 (2021) 104727

Contents lists available at ScienceDirect

Journal of Wind Engineering & Industrial Aerodynamics

journal homepage: www.elsevier.com/locate/jweia

High-fidelity prediction of flight trajectories of plate-type debris in boundary layer winds

Dikshant Saini, Behrouz Shafei *

Department of Civil, Construction, and Environmental Engineering, Iowa State University, Ames, IA, 50011, USA

ARTICLE INFO

Keywords:
Windborne debris
Plate-type objects
Atmospheric boundary layer wind
Computational fluid dynamics
Rigid body dynamics
Flight trajectories

ABSTRACT

From reconnaissance surveys, plate-type objects, such as roof shingles and tiles, are known to be among the most common types of debris objects. Therefore, a reliable prediction of their flight trajectories is instrumental for evaluating the vulnerability of building envelopes, especially in the regions with severe windstorms. Despite the development of several quasi-steady models for this purpose, the current literature lacks high-fidelity models to predict the flight pattern and impact velocity of the windborne debris objects separated from the ground and/or buildings. To address this gap, a coupled computational fluid dynamics and rigid body dynamics simulation framework was developed in the current study to capture the flight trajectories of plate-type debris objects in atmospheric boundary layer winds. Upon establishing a fundamental understanding of main flight characteristics, this study was extended to investigate the effects of initial pitch and yaw angles, plate characteristics, mean wind velocity, and release height on the flight of plate-type debris. In addition, a set of models were developed to predict debris travel distance, as well as linear and angular velocities associated with it. This can be directly employed to assess the impact-induced loading demand that building envelopes are expected to resist due to windborne plate-type debris.

1. Introduction

Windborne debris objects, which often originate from partially-fixed or damaged building components, have been identified as a main source of damage to building envelopes during hurricanes and tornadoes. Among the past reconnaissance surveys, Reed (1970) reported windborne debris as the primary source of damage to the windows of high-rise buildings during Lubbock Storm (1970). The damage surveys conducted after Hurricane Celia (1970) also revealed that the breakage of windows in downtown Corpus Christi, Texas, was mainly due to windborne debris impact. Pieces of roof were particularly observed as glass-breaking agents (Minor, 1994). Widespread damage from windborne debris impact was also notable in Tropical Cyclone Tracy (1974) in Darwin, Australia. Beason et al. (1984) investigated the damage caused by Hurricane Alicia (1983) in Houston, Texas, and reported that windborne missiles originated from building roofs were the primary cause of damage to architectural glazing systems. It was also determined that the building envelope failures caused by windborne debris often occur before the wind-induced lateral pressure becomes critical. Oliver and Hanson (1992) reported that debris impact can shatter glazing components. The cited study also noted that the debris from roofing materials, especially clay and concrete roofing tiles, were the most common type of debris that caused damage to building envelopes. During Hurricane Charley (2004) and Hurricane Katrina (2005), asphalt shingles, roof tiles, and roof sheathing panels that had been separated from nearby buildings were the predominant source of windborne debris, which left extensive damage to several buildings and other structures (FEMA, 2006; FEMA, 2011). Similar observations were made regarding the role of windborne debris as the primary cause of damage to building envelopes during a derecho in the Midwest of the United States in 2020.

Windborne debris hazard can be investigated in the three stages of generation, flight, and impact. The current study focuses on the flight stage, which is critical to not only characterizing the flight trajectories of debris and their locations of impact, but also to quantifying the impact velocity and kinetic energy that building envelopes are expected to experience. In the 1970s, a few studies were carried out on debris flight patterns, primarily focusing on tornado-borne debris (e.g., Lee, 1974; Stephenson et al., 1978; Twisdale et al., 1979). Later, additional studies were conducted on windborne debris flights in straight-line winds.

* Corresponding author.
E-mail addresses: dikshant@iastate.edu (D. Saini), shafei@iastate.edu (B. Shafei).

https://doi.org/10.1016/j.jweia.2021.104727
Received 6 January 2021; Received in revised form 10 July 2021; Accepted 15 July 2021
Available online 6 August 2021

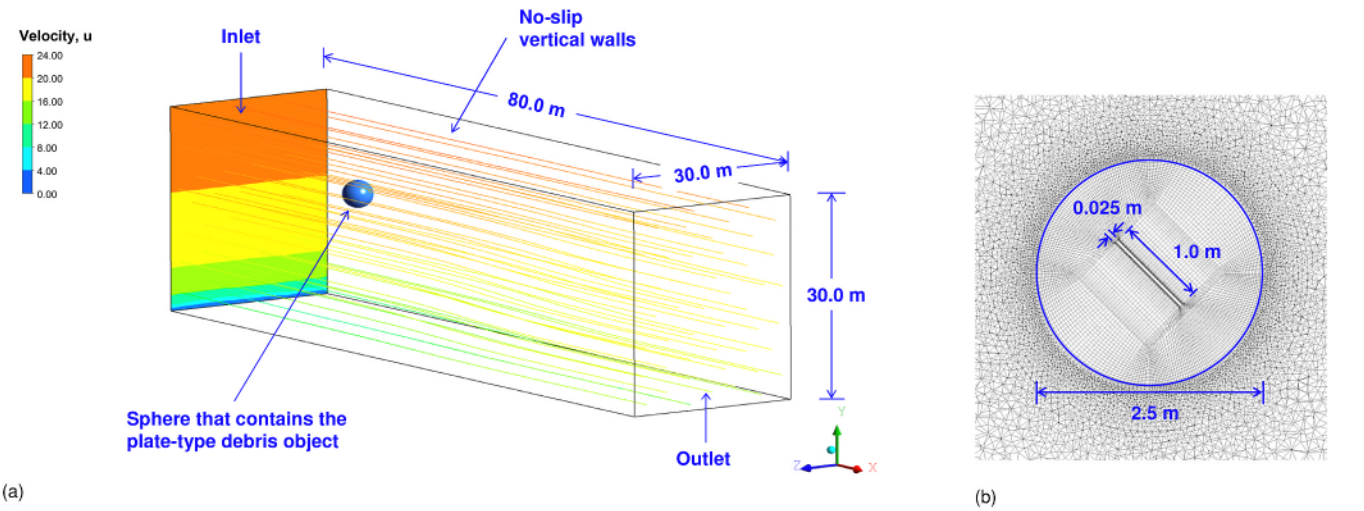

Fig. 1. CFD-RBD simulation environment: (a) the computational domain developed for debris flight, and (b) a cross-sectional view, reflecting the mesh pattern in the vicinity of the plate.

Among them, Tachikawa (1983) performed wind tunnel experiments and measured the drag, lift, and moment force coefficients on rotating plates in a uniform flow. Experimental expressions for these coefficients were developed as a function of rotational velocity. In particular, a dimensionless parameter, i.e., ratio of aerodynamic to gravity force, was introduced as the principal determinant of debris trajectory. In a separate effort, Holmes (2004) studied the trajectories of spheres carried by strong winds. It was identified that the effect of vertical air resistance must be considered to accurately predict both horizontal and vertical components of debris flight. Lin et al. (2007) investigated the trajectories of compact and rod-type windborne debris in horizontal winds. The cited study reported that the ratio of the horizontal velocity of a debris to the wind gust is essentially a function of the horizontal distance traveled by the debris, as it accelerates in the wind direction. Visscher and Kopp (2007) investigated the separation and flight of a sheathing panel, as a representative debris commonly observed in North America. The study determined how a plate-type debris can experience a range of auto-rotational, translational, and intermediate modes of flight. Richards et al. (2008) conducted wind tunnel experiments on rectangular plates and rods with different aspect ratios. The study explained how the force coefficients depend on both attack and tilt angles.

The current body of knowledge on debris flight patterns can be broadly divided into experimental tests (e.g., Tachikawa, 1988; Lin et al., 2006; Visscher and Kopp, 2007; Richards et al., 2008; Kordi et al., 2010; Kordi and Kopp, 2011), analytical studies (e.g., Lee, 1974; Redmann et al., 1978; Twisdale et al., 1979; Tachikawa, 1983; Wills et al., 2002; Holmes et al., 2006; Baker, 2007; Lin et al., 2007; Richards et al., 2008; Noda and Nagao, 2010; Grayson et al., 2012; Baker and Sterling, 2017), and computational efforts (e.g., Murakami et al., 1987; Andersen et al., 2005; Murman et al., 2005; Costello et al., 2007; Jin and Xu, 2008; Kakimpa et al., 2010; Kakimpa, 2012; Kakimpa et al., 2012a; Kakimpa et al., 2012b). Despite the valuable contributions of the cited studies, there are still open questions regarding the flight patterns of windborne debris. Among them is capturing the complex autorotation of windborne objects. Most of the existing studies have focused on a fixed-axis, two--dimensional (2D) autorotation. However, windborne debris objects are often found to exhibit three-dimensional (3D) spinning modes of autorotation. During the flight, a debris can interact with its own wake or with the vortex structure created by surrounding buildings (Andersen et al., 2005). The wake effects are known to be pronounced, especially in the release and initial stages of debris flight. The available analytical models, however, fall short to account for these effects. For plate-type objects, in particular, it has been noted that the quasi-steady torque used in the analytical models can significantly differ from the aerodynamic torque measured from the autorotation of flat plates (Martinez-Vazquez et al., 2010). To address such shortcomings, high-fidelity simulations are essential to take into consideration the release and flow conditions that debris objects commonly experience.

Among possible simulation strategies, coupled computational fluid dynamics (CFD) and rigid body dynamics (RBD) simulations have gained attention in the aerospace domain, especially for debris transport analysis during shuttle ascent (Murman et al., 2005; Brown et al., 2006). The current study capitalizes on the capabilities of the CFD-RBD models to provide a detailed insight into the trajectories of plate-type debris objects. Specifically, this advances the last study published on this subject (Kakimpa, 2012), which was focused on square plates under low-turbulence uniform wind fields. Among the original contributions of the current study is making a transition from uniform wind fields to atmospheric boundary layer (ABL) winds. This study also goes beyond a square plate by considering both square and rectangular plate-type objects. The developed CFD-RBD simulation framework investigates the dynamic motion of the plate-type objects using the RBD solver, which receives pressure forces from the CFD solver paired with it. A unique capability of this framework is to require no prior knowledge of debris aerodynamics, as the entire process is directly simulated. In this paper, Section 2 provides a detailed description of the simulation framework and supporting assumptions. Section 3 presents model validation details, which build on the past analytical and experimental studies. Section 4 discusses the free flight trajectories of square plates in ABL winds with various initial conditions, including a wide range of pitch and yaw angles. Section 5 extends the study to evaluate the effects of key input parameters, such as plate characteristics, mean wind velocity, and release height, on debris flight trajectories. Finally, Section 6 provides a set of predictive models developed based on the simulation results to obtain a high-fidelity assessment of debris travel distance, as well as linear and angular velocities associated with it. With the determination of the velocity (and subsequently the kinetic energy) of debris objects, this study contributes to providing an important input for the design and assessment of building envelopes that can adequately resist the windborne debris hazard (Kulkarni and Shafei, 2021; Saini and Shafei, 2020a,b, 2021).

2. Description of CFD-RBD simulation framework

The base CFD model consisted of a square plate with a length of 1.0 m and a thickness of 0.0254 m in a rectangular prism domain of 80.0 m (length) × 30.0 m (width) × 30.0 m (height). Fig. 1 shows the modeled computational domain, along with a section of the structured mesh

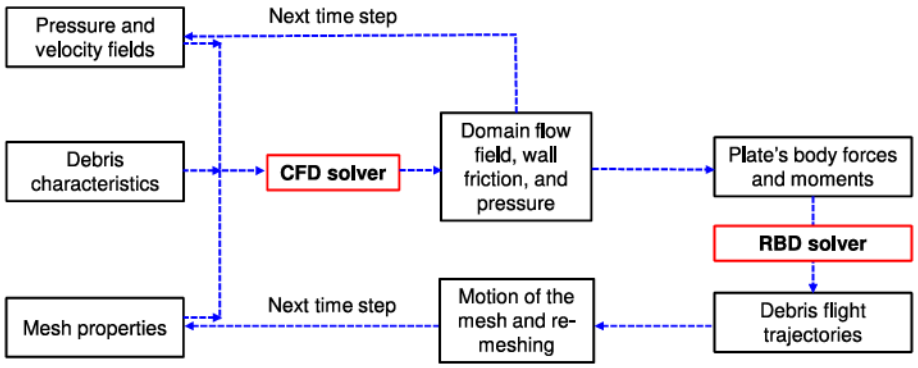

Fig. 2. Details of the sequential coupling of CFD and RBD solvers.

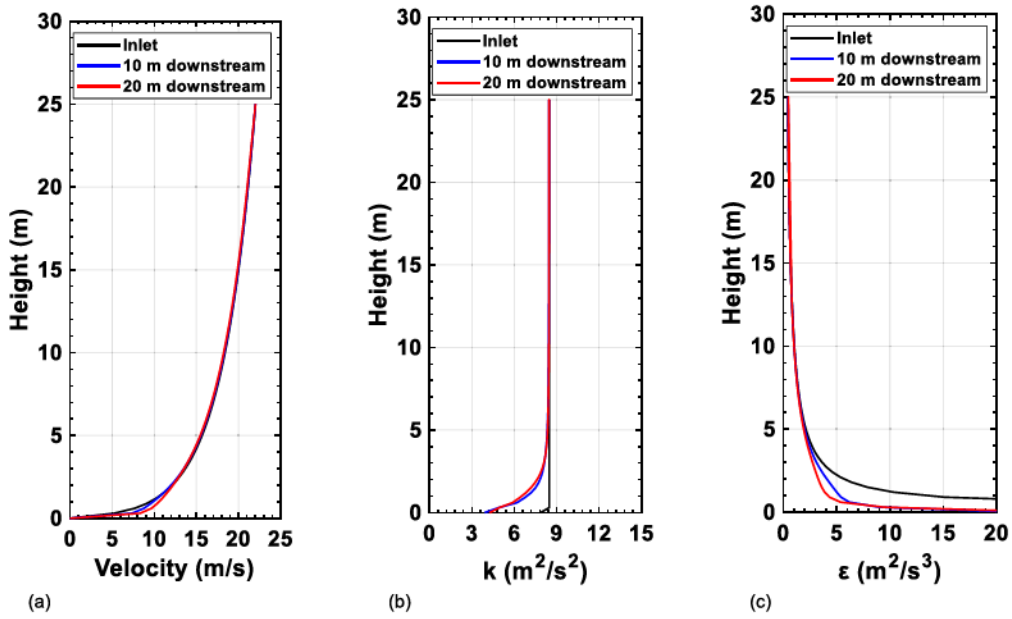

Fig. 3. Profiles of the wind flow characteristics at three sections: (a) horizontal component of the wind velocity, (b) turbulence kinetic energy, and (c) turbulence dissipation rate.

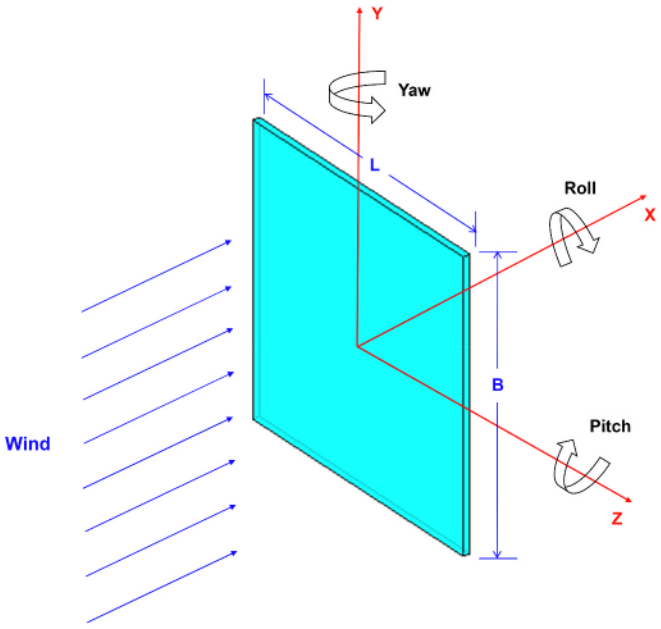

Fig. 4. A schematic sketch of the plate's angular movements in the wind flow.

around the plate. The x-axis was aligned in the along-wind direction; the y-axis was assumed in the vertical direction; and the z-axis was aligned in the across-wind direction. The plate was positioned inside a spherical region of diameter 2.5 L, where L is the plate's length. This diameter was deemed adequate because the main purpose of such a discretization was to allow the plate's movement without having to remesh its surrounding region. The spherical region was non-deformable and coupled with the plate, which was initially placed 10.0 m downstream the inlet in the x direction, 15.0 m away from the vertical side walls, and 15.0 m above the base surface. The base surface was modeled as a rigid surface with no slip, whereas the vertical side walls were modeled with a symmetry condition, in which the shear stress was zero. The top surface was modeled as a boundary with the mean wind velocity, turbulence kinetic energy, and turbulent energy dissipation rate calculated using the velocity and turbulence profiles provided at the inlet. The computational domain was discretized into a total of 2.8×10^6 cells. As shown in Fig. 1 (b), a structured mesh was used in the spherical region, while an unstructured mesh was adopted outside the sphere. As the plate moves in the 3D space, the linear and angular displacements can cause mesh distortion. Thus, the mesh in the spherical region was kept fixed and perfectly coupled with the plate during the motion. The region outside the sphere, however, was re-meshed at every time step to maintain the quality of the mesh, in terms of skewness and length scale. A velocity profile was assigned to the inlet, while a constant pressure boundary was

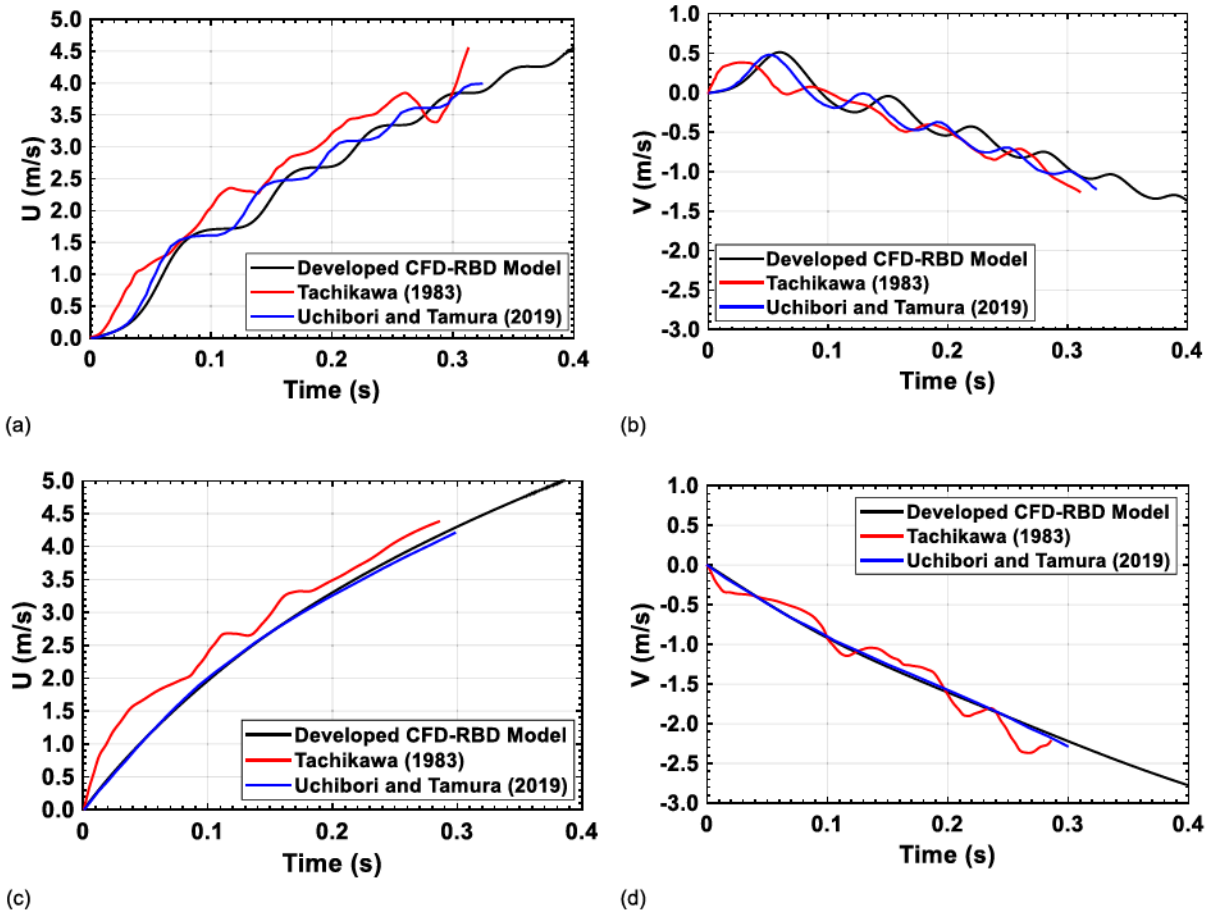

Fig. 5. Comparison of the translational velocities in the horizontal, U, and vertical, V, directions for the square plate with an initial pitch angle of (a),(b) 15°, and (c), (d) 90°.

maintained at the outlet. The ANSYS FLUENT software package was utilized to solve the unsteady incompressible Navier-Stokes equations and simulate the flow field around the plate-type debris. In turbulent flows, pressure and velocity profiles exhibit temporal variations. This was resolved in the developed model using a Reynolds decomposition to represent the flow variables, including the instantaneous pressure and velocity. The instantaneous variable (v_i) was decomposed into a time-averaged component (V_i) and a fluctuating component (v_i'). After combining the 3D Navier-Stokes equations with the Reynolds decomposition applied to the flow variables, the 3D Reynolds-Averaged Navier-Stokes (RANS) equations were obtained. Equation (1) expresses the continuity equation, while Equation (2) represents the momentum conservation equation.

$$\frac{\partial U_i}{\partial x_i}=0 \tag{1}$$

$$\rho\frac{\partial U_i}{\partial t}+\rho U_j\frac{\partial U_i}{\partial x_j}=-\frac{\partial P}{\partial x_i}+\frac{\partial}{\partial x_j}\left[\mu\left(\frac{\partial U_i}{\partial x_j}+\frac{\partial U_j}{\partial x_i}\right)-\rho\overline{u_j'u_i'}\right] \tag{2}$$

where U_i and u_i' are the instantaneous time-averaged and fluctuating velocity in the x_i direction, respectively; P is the time-averaged static pressure; μ is the fluid's dynamic viscosity assumed as 1.789×10^{-5} kg/m.s; ρ is the air density assumed as 1.225 kg/m^3, in accordance with the International Standard Atmosphere; and t is the time. The $-\rho\overline{u_j'u_i'}$ term is known as the Reynolds stress tensor, often denoted by τ_{ij}, where i and j subscripts represent the corresponding directions. For modeling the turbulence, the Realizable k-ε model with scalable wall functions was employed in this study. A second-order discretization scheme was used for both convection and viscous terms of the governing equations. For pressure interpolation from the center to the faces of each cell, a second-order interpolation scheme was utilized.

For capturing the flight trajectories of windborne debris, the RBD model was essential to define the debris motion in the 3D space. This motion can be in six degrees of freedom, i.e., translation along the three orthogonal axes and rotation about the three orthogonal axes. Based on the principles of conservation of linear and angular momentum, the RBD can be modeled using the following set of differential equations:

$$m\left(\frac{dv_G}{dt}\right)=F_G \tag{3}$$

$$I_D\frac{d\omega_D}{dt}=M_D-\omega_D\times I_D\omega_D \tag{4}$$

where m is the mass of the debris; I_D is the moment of inertia of the debris about the three principal axes; v_G is the translational velocity vector at the center of gravity of the debris; F_G is the vector of the aerodynamic force acting at the center of gravity of the debris; ω_D is the angular velocity vector; and M_D is the vector of the aerodynamic moment. While the aerodynamic force (F_G) and aerodynamic moment (M_D) are obtained from the CFD simulations, the second term on the right hand side of Equation (4) captures the calculations required in the rotating frame of reference. This term is important because both the moment of inertia and angular velocity of the debris change during the debris flight in the 3D space. Fig. 2 presents a flowchart, demonstrating the sequential coupling of the developed CFD and RBD solvers, similar to

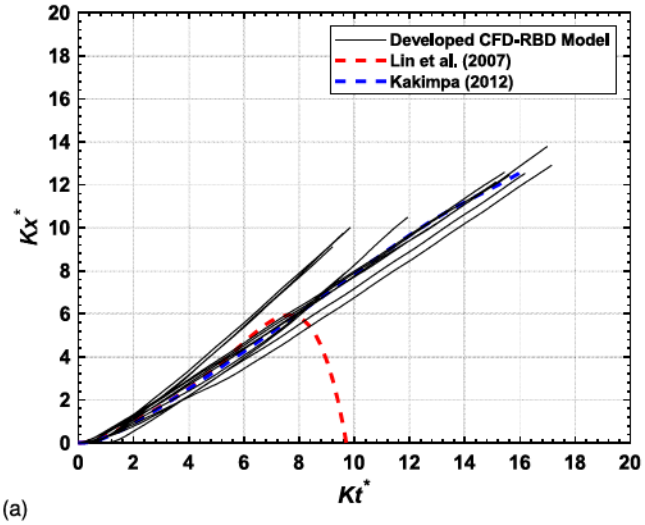

(a)

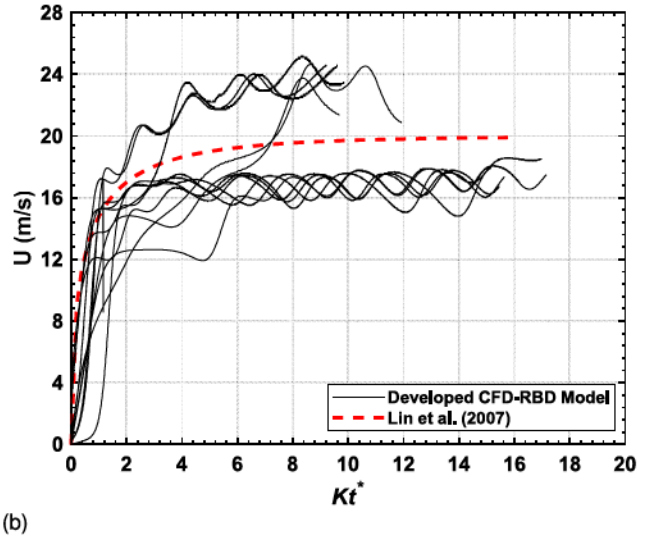

(b)

Fig. 6. Mean flight trajectories obtained for the square plate with a range of initial pitch angles from 0° to 165°: (a) comparison of the recorded non-dimensional horizontal displacements to those reported in Lin et al. (2007) and Kakimpa (2012), and (b) comparison of the horizontal translational velocities with those provided in Lin et al. (2007). Multiple lines of the same color represent various initial pitch angles. (For interpretation of the references to color in this figure legend, the reader is referred to the Web version of this article.)

Kakimpa et al. (2010).

In a departure from the previous studies, which were primarily focused on capturing debris flight trajectories in uniform winds, the current study makes a transition to ABL winds. For the k-ε turbulence models, Richards and Hoxey (1993) proposed the equations for the vertical profile of the mean wind speed, U, turbulence kinetic energy, k, and turbulence dissipation rate, ε, in an ABL wind. Thus, the mean wind speed was estimated by the following equations at the height of z:

$$U = \frac{u_*}{k}\ln\left(\frac{z+z_0}{z_0}\right) \tag{5}$$

$$u_* = \frac{u_{\mathrm{ref}}\mathrm{k}}{\ln\left(\frac{z_{\mathrm{ref}}+z_0}{z_0}\right)} \tag{6}$$

where u_* is the friction velocity; k is the von Karman's constant; z_0 is the surface roughness; and u_{ref} is the velocity at the reference height of z_{ref}. The turbulence kinetic energy, k, and the turbulence dissipation rate, ε, were determined by Equations (7) and (8), respectively:

$$k = \frac{u_*^2}{\sqrt{C_\mu}} \tag{7}$$

$$\varepsilon = \frac{u_*^3}{k(z+z_0)} \tag{8}$$

where C_μ is a constant in the k-ε turbulence model. In addition to the inlet conditions, the equivalent sand roughness height, k_s, for ABL winds was calculated using the following equation:

$$k_s = \frac{9.793 z_0}{C_s} \tag{9}$$

where C_s is the roughness constant; and z_0 is the roughness length. In the current study, a roughness length of 0.1 m was considered. This represents a rough, open terrain, as outlined in Simiu and Scanlan (1978) and ESDU (1990). This assumption was made following the study conducted by Visscher and Kopp (2007) on the flight trajectories of plates. Preliminary simulations were performed to compare the flow field at different locations along the modeling domain. For a mean wind velocity of 20 m/s, the velocity profile, turbulence kinetic energy, and turbulence dissipation rate were compared at multiple locations, including at the inlet, 10.0 m downstream the inlet, and 20.0 m downstream the inlet (Fig. 3). This figure shows that the profiles were consistent at the three locations, except for some differences in the turbulence kinetic energy and turbulence dissipation rate near the ground. Such differences, which are due to the limitations of the standard wall functions, can be minimized by further refining the mesh near the ground. However, their effect on the recorded debris flights was determined to be so marginal that the extra computational time was not justified. It must be noted that the actual flow in real-world extreme wind events is fully turbulent, in which the wind speed and direction vary with time. Based on the profiles presented in Fig. 3, the turbulence intensity was found to be 12%, which falls well in the range of 10%–20% observed in high-turbulence wind flows.

3. Validation of developed models

Prior to the main simulations, the developed framework was validated with the analytical and experimental studies performed in the past. The first validation was with the trajectories of square flat plates obtained from a set of wind tunnel experiments (Tachikawa, 1983) and numerical simulations (Uchibori and Tamura, 2019). For this purpose, a 0.04 m × 0.04 m plate with a thickness of 0.002 m was released into a uniform wind flow at various initial pitch angles. Fig. 4 illustrates the plate's angular displacements in the wind flow. A pitch angle of 90° implies that the flow is normal to the face of the plate. The modeled computational domain had a dimension of 2.00 m in the wind stream direction, 0.85 m in the width, and 0.85 m in the height. The centroid of the plate was placed 0.425 m away from the inlet. A uniform wind velocity of 9.2 m/s (Re = 24,500) was applied to the inlet with a length scale and turbulence intensity of 0.01 m and 2%, respectively. The plate was held fixed in its original orientation for 0.05 s to allow for the generation of vortices behind it. The plate was then released and the flow-induced free flight trajectories were calculated using the procedure defined in Section 2. A fine mesh with an average cell size of L/320 (where L is the plate's length) was used around the plate. The mesh size was then gradually increased away from the plate's surfaces. The inner sphere had an average mesh size of L/100. A representation of the mesh sizes used in the simulations is shown in Fig. 1(b).

For validation purposes, the free flight motion of the square flat plate was investigated at two initial pitch angles of 15° and 90°. These two pitch angles helped validate the simulation results for two different

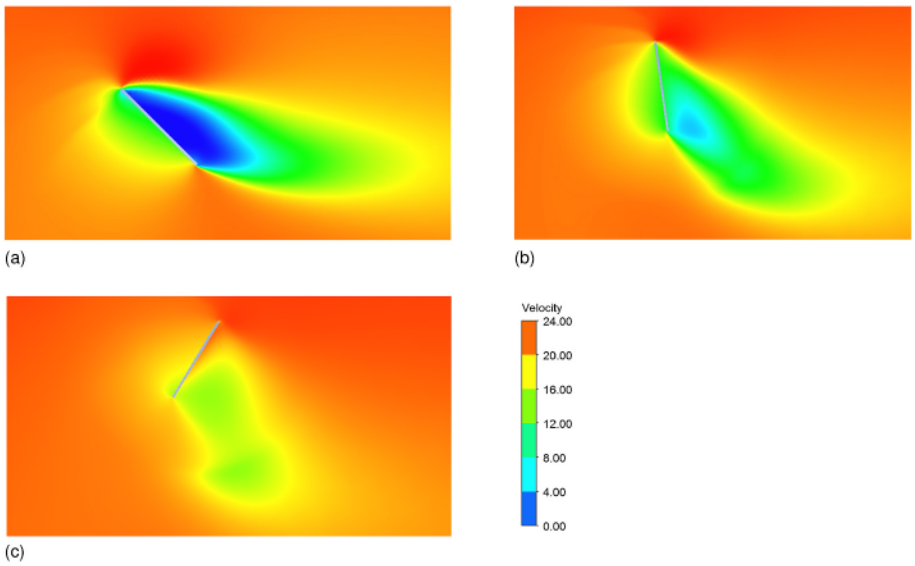

Fig. 7. Velocity contours around the square plate with an initial pitch angle of 45° after (a) 0.0 s, (b) 0.2 s, and (c) 0.4 s.

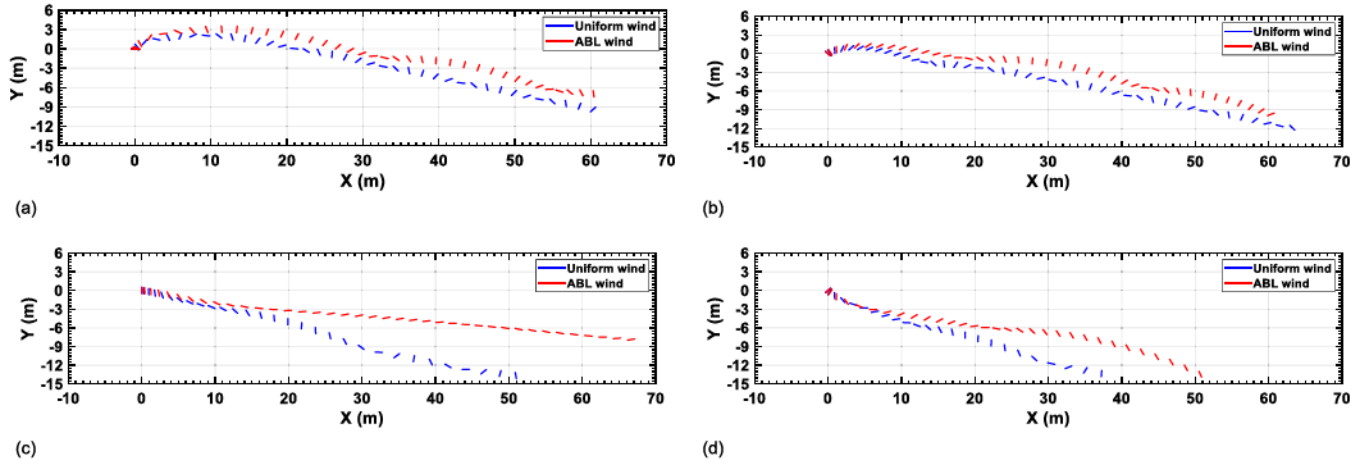

Fig. 8. Comparison of the mean flight trajectories in the uniform and ABL wind under an initial pitch angle of (a) 0°, (b) 45°, (c) 90°, and (d) 135°.

types of trajectories, i.e., with and without rotation. The simulated flight trajectories were first examined using the velocity time histories in the along-wind and downward directions. Next, the aerodynamic characteristics of the free flights were extracted and compared. Fig. 5 shows the translational velocities of the plate measured at its center of gravity, in comparison to the experimental test and numerical simulation results. The velocity profiles reported from the experiments were obtained by curve fitting, consistent with Uchibori and Tamura (2019). For an initial pitch angle of 15°, the velocities were found to fluctuate with time, as a result of the plate's autorotation. The CFD simulations closely captured the fluctuations, similar to those provided in Tachikawa (1983) and Uchibori and Tamura (2019). On the other hand, the velocity time histories did not show any fluctuations for the case with an initial pitch angle of 90°, confirming that no autorotation occurs. In addition, the aerodynamic characteristics of the plate's free flight were investigated at every 0.025 s. The CFD simulations were found to closely replicate those characteristics, reflecting the accuracy of the developed CFD-RBD model.

To extend model validation to the plate sizes that represent large plate-type debris, the second set of investigations in the current study focused on the free flight trajectories of a square plate with the dimensions of 1.0 m × 1.0 m and a thickness of 0.0254 m. This plate can well represent large roofing sheets separated from buildings during extreme wind events. Various grid sizes were first examined in preliminary simulations to ensure that the main simulation results remain grid independent. Upon evaluating the plate's drag, lift, and moment coefficients, a mesh size of L/320 (where L is the plate's length) was decided to ensure a close agreement of the plate's aerodynamic coefficients with the experimental test results (ESDU, 1970). Outside the sphere, the mesh size was gradually increased to reduce the computational time. Prior to the main simulations, additional investigations were conducted to ensure that the simulation results also remain independent of time step. From the sensitivity analyses conducted for this purpose, a time step of 0.002 s was adopted. The flight trajectories were simulated for 4.0 s at a wind velocity of 20 m/s ($Re = 1.3 \times 10^6$). The wind velocity was applied to the inlet with a length scale of 0.1 m and a turbulence intensity of 2%. The plate was initially held fixed in its original orientation for 2.5 s. This allowed the full development of the flow field and vortices around the debris object.

A set of simulations were performed to study the effects of initial pitch angle on debris flight trajectories. For each simulation case, all the displacement and velocity components were recorded as a function of

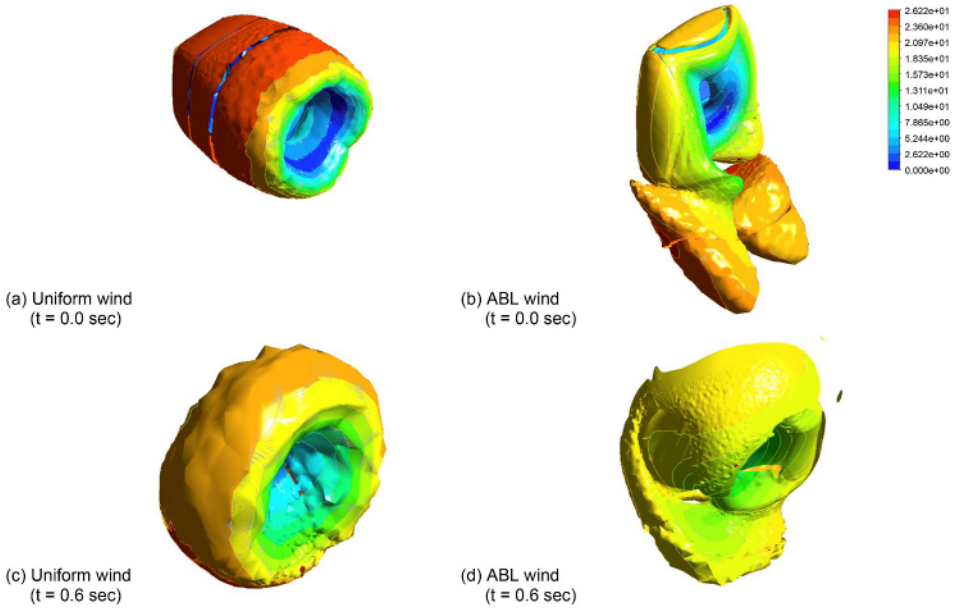

Fig. 9. Instantaneous iso-surfaces of Q-criterion, showing the CFD-predicted velocity contours (m/s) in the wake of the plate under the uniform and ABL flow fields.

time. For validating the developed simulation framework, the flight trajectories were compared to the predictions from Lin et al. (2007) and Kakimpa (2012). The debris flight trajectories were represented using the non-dimensional horizontal distance ($Kx^* = Kxg/U^2$) against the non-dimensional time ($Kt^* = Ktg/U$), where K is the Tachikawa number defined using the following equation:

$$K = \frac{\rho U^2 A}{2mg} \tag{10}$$

where ρ is the air density assumed as 1.225 kg/m^3, in accordance with the International Standard Atmosphere; A is the plate's surface area, which is 1.0 m^2; m is the plate's mass assumed equal to 3.0 kg; U is the mean wind speed at the elevation of the debris; and g is the acceleration due to gravity, which is taken as 9.81 kg/m^3. Fig. 6(a) presents the flight trajectories for an initial pitch angle that range from 0° to 165° (in 15° intervals). The plate's flight trajectory was sensitive to the initial pitch angle, as reflected in the wide range of recorded horizontal travel distances. The obtained trajectories were observed to properly capture the range of predictions provided by Lin et al. (2007) and Kakimpa (2012). It must be noted that the formula provided in Lin et al. (2007) comprises of a polynomial function, in which with the increase of Kt^*, Kx^* consistently increases until a sudden drop occurs. Therefore, the referenced expression is only valid for Kt^* less than 7.5. As shown in Fig. 6(b), depending on the initial pitch angle, the plate's maximum horizontal velocity was 0.75–1.25 times of the mean wind velocity. From a detailed comparison of the simulation results to the available experimental and numerical data, the developed CFD-RBD simulation framework was found to be accurate enough to characterize the flight trajectories of plate-type debris objects.

4. Flight trajectories of plate-type debris in ABL winds

The flight trajectories of a square plate with the dimensions of 1.0 m × 1.0 m and a thickness of 0.0254 m were evaluated under ABL winds. The first set of simulations were similar to those presented in the validation investigation, but with a transition from a uniform to an ABL wind. For each simulation, the plate was held fixed in its original orientation for 2.5 s to allow for the generation of vortices behind it. Fig. 7 presents the velocity contours around the square plate after its release in the ABL wind. For each simulation, the plate's translational and angular velocity components were recorded. To properly understand the effects of ABL winds on the flight pattern of plate-type objects, side-by-side comparisons were made on the trajectories and velocity profiles obtained from the uniform and ABL winds. For both simulation cases, the plate's initial location was assumed to be 15.0 m above the ground, where the mean wind velocity was 20.0 m/s (i.e., a Tachikawa number of 8.33). Fig. 8 shows the plate's flight trajectories in the uniform and ABL winds for the initial pitch angles of 0°, 45°, 90°, and 135°. The plate's position in the x-y plane was plotted at 0.1 s time intervals. This figure clearly shows that the ABL wind has a significant influence on the plate's flight trajectories.

For the initial pitch angle of 0°, the plate was found to travel farther in the ABL wind than in the uniform wind for the same vertical distance. In addition, the plate in motion experienced much higher lift forces at the time instances that the pitch angle became 0°/180°. This observation was also evident in the plate flights recorded for the other initial pitch angles. For the initial pitch angle of 90°, the plate trajectories in the ABL wind were determined to have significant differences from those in the uniform wind. For the traveled horizontal distance of 50.0 m, the plate was observed to travel 6.0 m downwards in the ABL wind, as compared to more than 12.5 m in the uniform wind. The differences in flight trajectories were further studied by analyzing the flow field in the wake of the plate. Fig. 9 shows the three-dimensional flow structures in the wake of the square plate released with an initial pitch angle of 90°. In this figure, a Q-criterion has been employed to visualize the vortex cores. The flow around the plate in the uniform wind was observed to be much more symmetric than that in the ABL wind. The negative velocities behind the plate under the uniform wind were also consistently higher than those under the ABL wind. From the simulations with the uniform wind, the main vortices were near vertical at the time of release and then merged together to form a stable ring. On the other hand, the flow structure in the ABL wind was composed of the edge vortices that led to an asymmetrical flow structure. Similar observations were made during the simulations that involved the other initial pitch angles (ranging from 0° to 165° with the intervals of 15°), reflecting how the risk of windborne debris impact could be underestimated if the simulations had been limited to a uniform wind. This highlighted one of the main contributions of the current study, which utilized ABL wind simulations for achieving improved accuracy.

Following the review of the recorded flight trajectories, the ABL wind effects on the horizontal, U, and vertical, V, velocity components of the

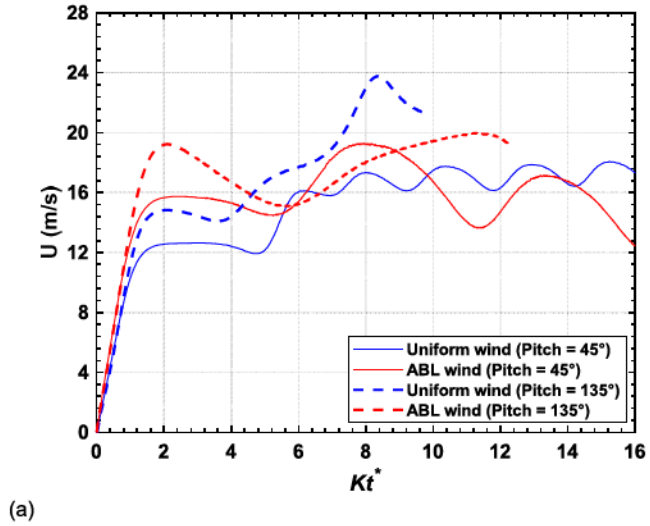

(a)

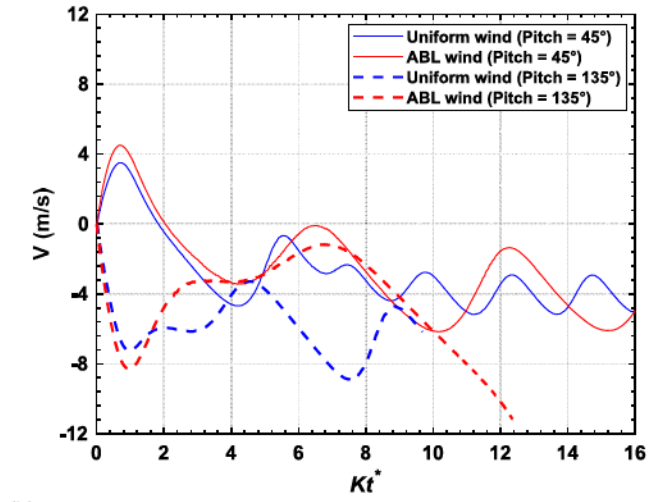

(b)

Fig. 10. Comparison of (a) horizontal and (b) vertical velocity of the plate object in the uniform and ABL wind with two different pitch angles.

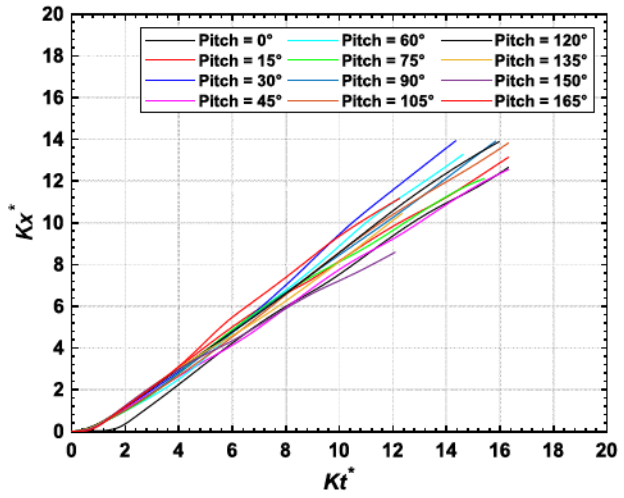

(a)

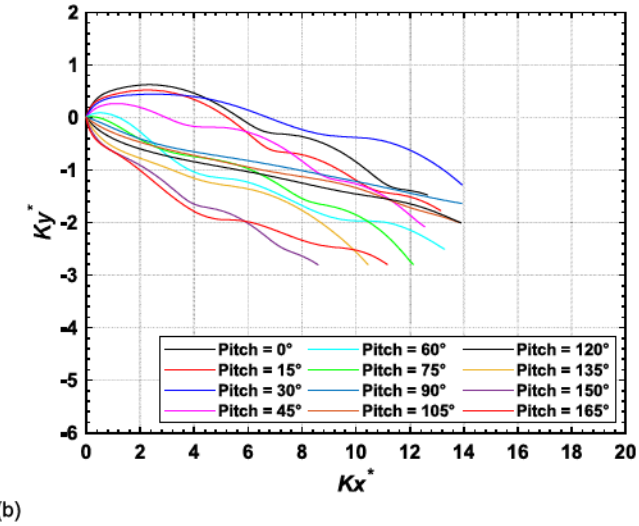

(b)

Fig. 11. Variation of mean flight trajectories for the plate with different pitch angles: (a) non-dimensional horizontal distance versus non-dimensional time, and (b) non-dimensional vertical distance versus non-dimensional horizontal distance.

plate were investigated. Fig. 10 presents a comparison of both velocity components under the uniform and ABL winds for the initial pitch angles of 45° and 135°. For the initial pitch angle of 45°, the maximum horizontal velocity was recorded to be 19.3 m/s in the ABL wind, as compared to 18.3 m/s in the uniform wind. However, the largest difference was observed in the cases that the initial pitch angle was 135°. A maximum horizontal wind velocity of 19.9 m/s was recorded in the ABL wind, while the same velocity reached 24.0 m/s in the uniform wind. A similar observation regarding the magnitude of the vertical velocities can be made in Fig. 10(b). To obtain a holistic perspective, the distributions of the horizontal and vertical distances traveled by the plate in the ABL wind were investigated as well. Fig. 11 presents the plate's trajectories, in terms of non-dimensional horizontal and vertical distances versus non-dimensional time. The obtained distributions reflected the strong sensitivity of the horizontal and vertical distances traveled by the plate to its initial pitch angle. Fig. 11(b) shows that the plate tended to move upward in some of the simulation cases, while this was reversed to the downward direction in the other simulation cases. This can be explained by the fact that the plate with an initial pitch angle less than 90° experiences a positive lift, while the same plate experiences a negative lift if the initial pitch angle exceeds 90°. The reported distributions are important, especially to identify the areas of a building envelope susceptible to windborne debris impact.

In the first set of simulations, the plates were observed to show negligible cross-wind motions, as the effect of yaw angle had not been included. Thus, the simulation cases were expanded to investigate the 3D motion of the plate-type debris with various yaw angles. For this purpose, five yaw angles, ranging from 15° to 75° (with the intervals of 15°), were simulated for each of the initial pitch angles of 15°, 30°, 45°, 60°, and 75°. This simulation matrix resulted in a total of 25 simulations. The distribution of plate trajectories in the x-z plane is shown in Fig. 12 for a plate's release height of 15 m and initial pitch angles of 15° and 75°. The plate was found to show a significant movement in the lateral z direction, depending on the yaw angle. As the horizontal distance traveled by the plate increased, the plate was also found to reverse its travel direction. Fig. 12(a) shows that the plate rapidly moved in the lateral direction when $Kx^* > 8$. To further understand the plate's 3D motion in the ABL wind, Fig. 13 presents the scatter plot of the plate's flight trajectories along a vertical section at 10.0 m, 20.0 m, and 30.0 m from the starting point in the x direction. Upon the release of the plate, the flight trajectory started to show a complex 3D pattern. In the early stage of the flight, i.e., $Kt^* < 2$, the lateral displacement increased with

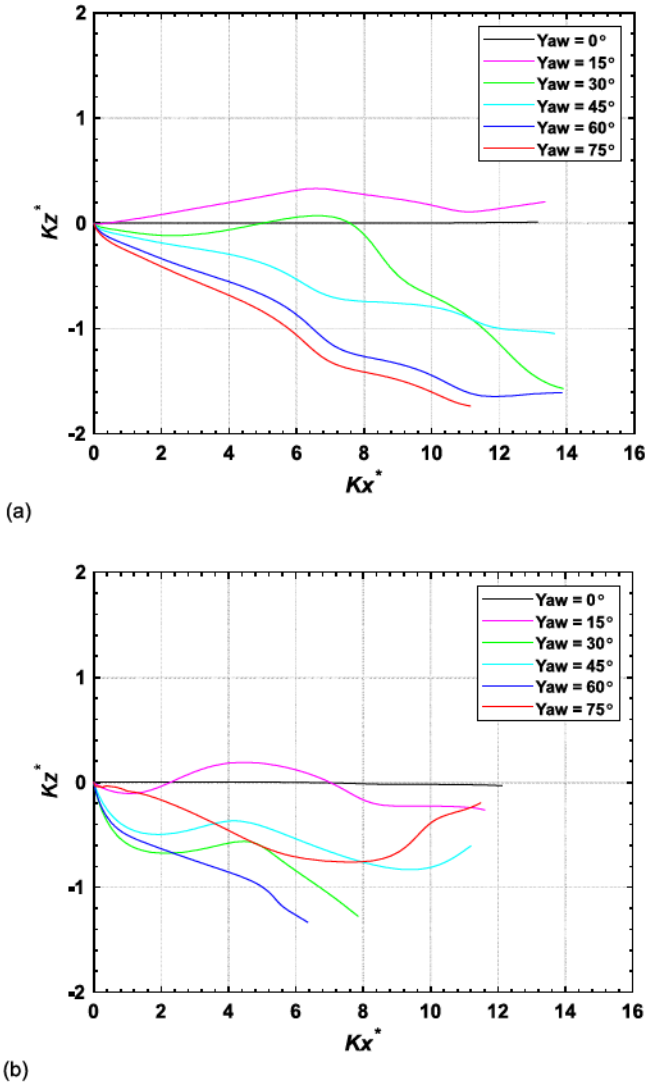

Fig. 12. Variation of mean flight trajectories in the lateral direction as a function of the horizontal distance traveled by the plate: (a) pitch angle = 15°, and (b) pitch angle = 75°.

the increase in the initial yaw angle. Further downstream, however, the plate was observed to traverse back in the lateral direction. Fig. 13(b) shows that the plate can move up to 6.0 m in the lateral direction even at a horizontal distance of 20.0 m from the release point. The scatter in the lateral movement of the plate increased further, as the plate moved in the along-wind direction. The lateral distance traveled by the plate reached a maximum of 7.0 m at the 30.0 m section downstream of the release point.

Fig. 14 presents the translational and angular velocity components of the plate during its flight under the ranges introduced for the yaw angles (with an initial pitch angle of 30°). The horizontal velocity was found to increase sharply to a level close to the mean wind velocity, i.e., 20 m/s. In particular, the plate tended to fly faster than the mean wind velocity in some of the simulation cases. This was primarily due to the plate's angular motion in those cases. Fig. 14(b) shows the plate's velocity component in the vertical direction. This velocity component increased sharply at the beginning and then decreased to almost half of its peak value. The plate in motion also rotated about its weak axis (i.e., z axis), which generated a rotational kinetic energy. The plate's angular velocities for various initial pitch and yaw angles are shown in Fig. 14(c). A positive value for the angular velocity represents an anti-clockwise

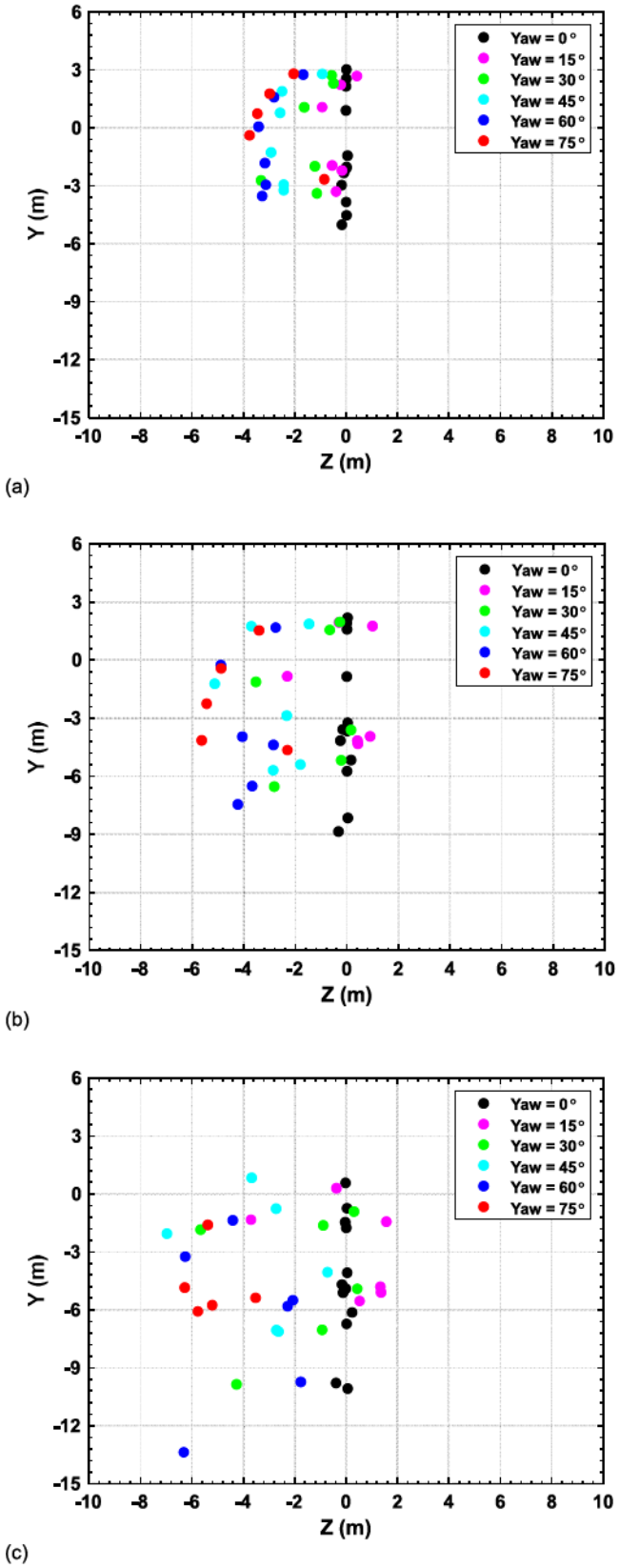

Fig. 13. Scatter plot of the mean flight trajectories with different pitch and yaw angles recorded at (a) 10.0 m, (b) 20.0 m, and (c) 30.0 m in the x direction from the starting point.

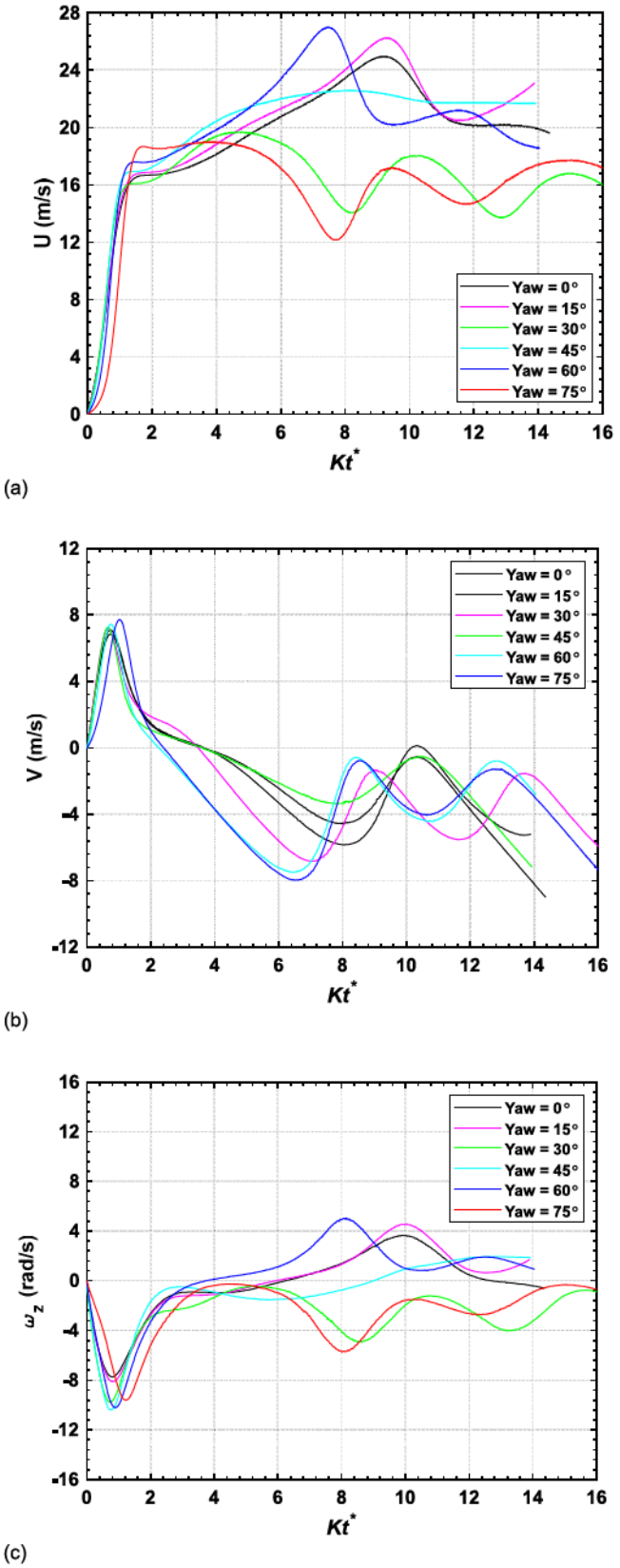

Fig. 14. Variation of the plate's velocity components over the course of the flight under an initial pitch angle of 30° and various yaw angles: (a) horizontal velocity, (b) vertical velocity, and (c) angular velocity.

rotation, while a negative value refers to a clockwise rotation. The angular velocity increased sharply during the release stage and then became stable over time. It is common to see that a plate experiences a transition from an anti-clockwise to a clockwise rotation (and vice versa) during its flight in the ABL wind. This is clearly reflected in Fig. 14(c), highlighting the importance of capturing the interactions between the plate and the surrounding wind.

5. Investigation of factors influencing debris flight

A comprehensive investigation of the parameters that directly influence the flight trajectories of plate-type objects in ABL winds was performed using the capabilities of the developed simulation framework. The selected parameters included: (i) plate characteristics, (ii) mean wind velocity, and (iii) release height. For each parameter, simulations were performed for the initial pitch angles, ranging from 0° to 165°. To study the effects of plate characteristics, three different plates made of balsa wood, wood, and slate were considered, capturing the most common roofing materials. The balsa wood plate had a dimension of 1.0 m × 1.0 m × 0.0254 m and a total mass of 3.0 kg, which can be representative of a large roofing sheet. A wood shingle with a surface size of 0.25 m × 0.61 m and a thickness of 0.0127 m was the second plate modeled with a total mass of 1.7 kg. The third plate was made of slate and had a surface size of 0.355 m × 0.610 m and a thickness of 0.0127 m with a total mass of 7.7 kg. For the second and third plates, the long side of the plate was assumed to be in the cross-wind direction. All the simulations were conducted with a release height of 15.0 m in an ABL wind with a mean wind velocity of 18.4 m/s (i.e., 20.0 m/s at the 15.0 m height). Under the introduced flow conditions, the Tachikawa number for the balsa wood roof panel, wood shingle, and slate tile were found to be 8.33, 2.24, and 0.70, respectively. Fig. 15 compares the flight trajectories of the three plates modeled using two initial pitch angles of 60° and 120°. The recorded flight patterns reflected how the trajectories can differ, depending on the mass and dimensional characteristics of the debris. The slate tile, which was the heaviest debris modeled in the current study, did not show a long flight and fell to the ground in an almost straight path. On the other hand, the wood shingle showed a significant rotational behavior from the very beginning, compared to the other two plate types, mainly because it had the lowest moment of inertia among the plate types considered. Although the wood shingle was the lightest debris modeled in the current study, the roof panel traveled farthest due to having the largest dimensions. In addition, because of their size, the slate tile and wood shingle did not experience a significant lift force, compared to the balsa wood roof panel. Based on the results obtained for the three plate-type debris objects, it is evident that the flight trajectory, in terms of distance traveled and debris orientation, is strongly dependent on the plate's inertial properties and Tachikawa number.

The effect of the mean wind velocity was investigated by performing additional simulations with a mean wind velocity of 25.0 m/s (i.e., 27.2 m/s at 15.0 m height) and 30.0 m/s (i.e., 32.6 m/s at 15.0 m height), further to 18.4 m/s (i.e., 20.0 m/s at 15.0 m height). The Tachikawa number for the new two velocities was determined to be 15.40 and 22.12, respectively. All the simulations were conducted using a plate with a surface size of 1.0 m × 1.0 m and a thickness and mass of 0.0254 m and 3.0 kg, respectively. Fig. 16 compares the flight trajectories of the modeled plate under different mean wind velocities with two initial pitch angles of 60° and 120°. In the early stage of the flight, the plate's displacement and orientation profiles were almost similar for the three mean wind velocities, although the plate tended to fly higher under a higher wind velocity. At 30.0 m downstream of the release point, the plate in the mean wind velocity of 30 m/s was 2.5 m below the release point, while the same plate was close to 6.0 m below the release point under the mean wind velocities of 18.4 m/s and 25.0 m/s. With increasing the mean wind velocity, the plate also showed (relatively) less rotation, which can be explained considering that the plate was

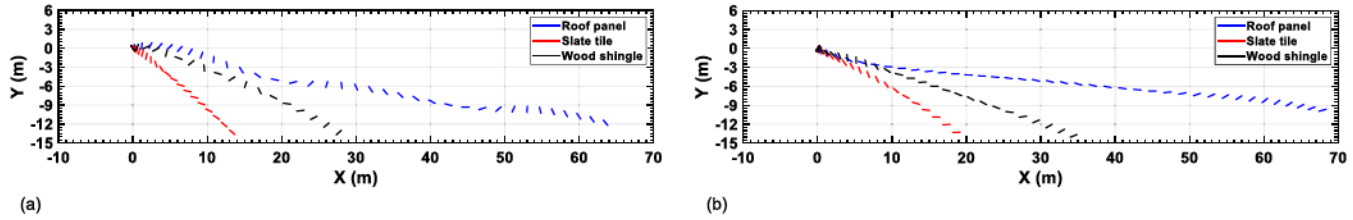

Fig. 15. Mean flight trajectories of the three plates modeled in the current study with the two initial pitch angles of (a) 60°, and (b) 120°.

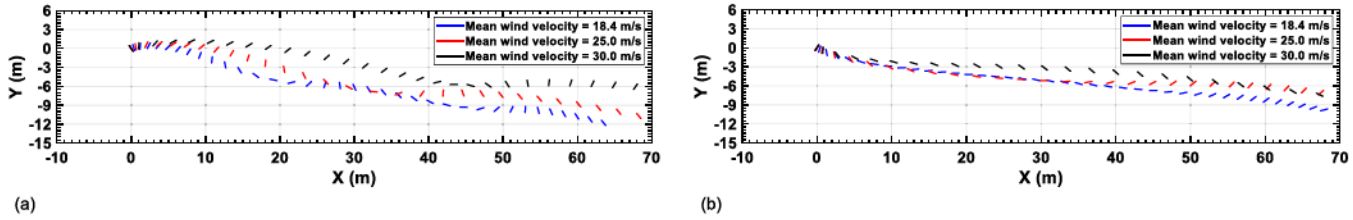

Fig. 16. Effect of the mean wind velocity on the mean flight trajectory of the square plate at the two initial pitch angles of (a) 60°, and (b) 120°.

moving at a higher horizontal velocity. The horizontal distance traveled by the plate also increased with the increase in the mean wind velocity.

The third parameter investigated in the current study was the release height. In addition to the original 15.0 m release height, a set of simulations were conducted to capture the flight of the roof panel with a release height of 10.0 m (i.e., a Tachikawa number of 7.05). Considering that the previous studies had utilized a uniform wind assumption, variation in the release height had been reported to not have a notable effect on the debris flight trajectory. In an ABL wind, however, the mean wind velocity changes over height, especially in the boundary layer. Fig. 17(a) compares the flight trajectories of the roof panel with two different release heights for initial pitch angles ranging between 0° and 165°. For the release height of 10.0 m, the mean of the horizontal distance traveled by the plate was observed to have a slightly lower slope than that obtained for the release height of 15.0 m. This revealed the importance of the Tachikawa number in defining the flight trajectory of a debris. Fig. 17(b) presents the plate's horizontal velocity for the two release heights, i.e., 10.0 m and 15.0 m. In the early stage of the flight, i.e., $Kt^* < 2$, the plate's velocity was observed to be similar for the two release heights. As the plate traveled farther, however, the mean velocities obtained for the simulations with a lower release height were confirmed to be consistently less than those obtained from the simulations with a higher release height.

6. Prediction of debris travel distance and impact velocity

For the risk analysis of building envelopes vulnerable to the windborne debris hazard, it is important to predict the horizontal distance traveled by debris objects, as well as their kinetic energy upon impact. In this study, the flight trajectories of square and rectangular plates (with a Tachikawa number, ranging from 0.70 to 22.12) were determined. In addition, the simulations covered a wide range of initial pitch and yaw angles, as well as flow conditions, including various mean wind velocities and release heights. Therefore, the wealth of data generated from the high-fidelity simulations performed in the current study was employed to develop a set of predictive equations. For this purpose, the non-dimensional horizontal trajectory of plate-type debris objects was expressed as a function of non-dimensional time. The data showed that the following equation can be used to predict the observed trajectory of various plate types in different flow conditions.

$$Kx^* = \frac{-0.027Kt^{*3} + 1.476Kt^{*2} + 1.377Kt^* - 0.319}{Kt^* + 4.905} \tag{11}$$

Fig. 18 shows the mean fit equation, along with 95% confidence bounds. The kinetic energy of the windborne debris is also essential to quantify the loading demand and corresponding damage to building envelopes. In the past models developed to calculate the risk of windborne debris impact, kinetic energy was evaluated only using the translational component of the wind velocity. However, in the debris flight, rotations also often occur, further increasing the impact energy. To capture both translational and rotational components, the kinetic energy of plate-type debris objects was calculated using the following equation:

$$KE = \frac{1}{2}mv_G^2 + \frac{1}{2}\left(I_{xx}\omega_x^2 + I_{yy}\omega_y^2 + I_{zz}\omega_z^2\right) \tag{12}$$

where I_{xx}, I_{yy}, and I_{zz} are the plate's moment of inertia about its x, y, and z axis, respectively; and ω_x, ω_y, and ω_z are the plate's angular velocity about its x, y, and z axis, respectively. From the presented investigations, the plates were observed to dominantly rotate about their z axis, which was aligned in the crosswind direction. Therefore, the angular velocity components about the x and y axes can be disregarded. Fig. 19 presents the scatter plot of the normalized horizontal velocity and normalized angular velocity, both as a function of non-dimensional horizontal distance for various plate types, mean wind velocities, and release heights. The horizontal velocities were normalized with a factor of U_H, where U_H is the mean wind velocity at the release height of the debris. On the other hand, the angular velocities were normalized with a factor of U_H/B, where B is the plate's width, as shown in Fig. 4. Due to the complex nature of debris flight, the horizontal velocity data demonstrated a large scatter. Therefore, two mean fit equations, along with their 95% confidence bounds, were developed using the simulation data to predict the normalized linear and angular velocity components, as follows:

$$U \Big/ U_H = 0.908\left(1 - e^{-\sqrt{4.662kx^*}}\right) \tag{13}$$

$$\omega_Z B \Big/ U_H = 0.175 - 0.40e^{-0.5kx^*} \tag{14}$$

Equations 11, 13, and 14 provide a prediction of the horizontal travel distance and the linear and angular velocity components of the plate-type debris objects in neutral, horizontally-homogenous ABL flow

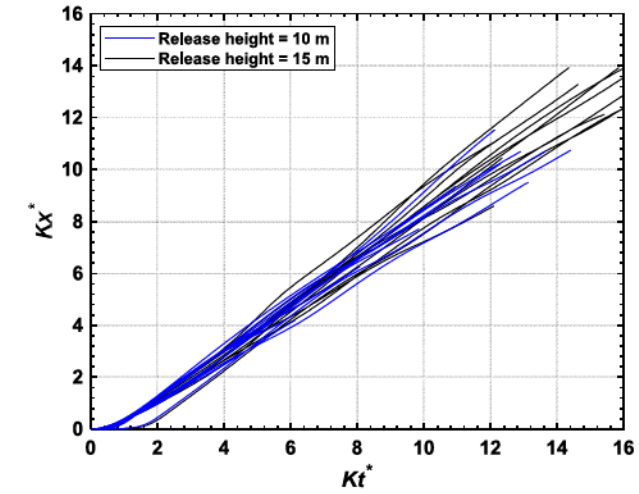

(a)

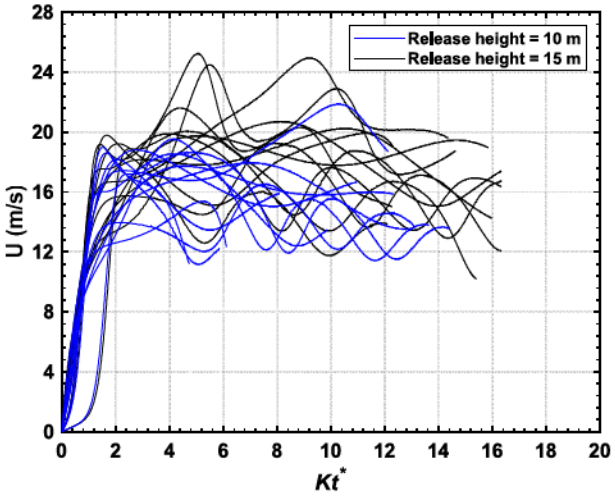

(b)

Fig. 17. Comparison of the mean flight trajectories of a square plate for two different release heights: (a) non-dimensional horizontal distance versus non-dimensional time, and (b) horizontal velocity versus non-dimensional time. Multiple lines of the same color represent various pitch angles. (For interpretation of the references to color in this figure legend, the reader is referred to the Web version of this article.)

conditions. The outcome of such predictive models helps evaluate the likelihood and intensity of windborne debris impact to building envelopes. This can guide the vulnerability assessment studies performed on building envelopes for hazard mitigation purposes.

7. Conclusions

This study investigated the flight trajectories of plate-type debris objects in ABL winds. For this purpose, high-fidelity CFD-RBD coupled simulations were conducted to capture the flight of various plates at a wide range of initial pitch and yaw angles. Prior to the main simulations, the CFD-RBD simulation framework was validated with the experimental test and numerical results. The CFD-RBD simulation framework was then extended from uniform to ABL winds. After completing the necessary validations, the simulation results successfully captured various debris flight characteristics, such as horizontal distance traveled by the debris, as well as the linear and angular velocities associated with it. The main conclusions drawn from the presented study are as follows:

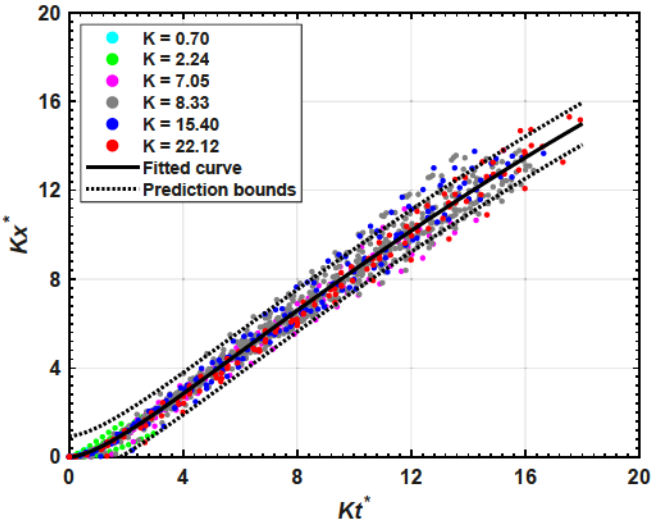

Fig. 18. Non-dimensional horizontal trajectories of the plate-type objects as a function of non-dimensional time.

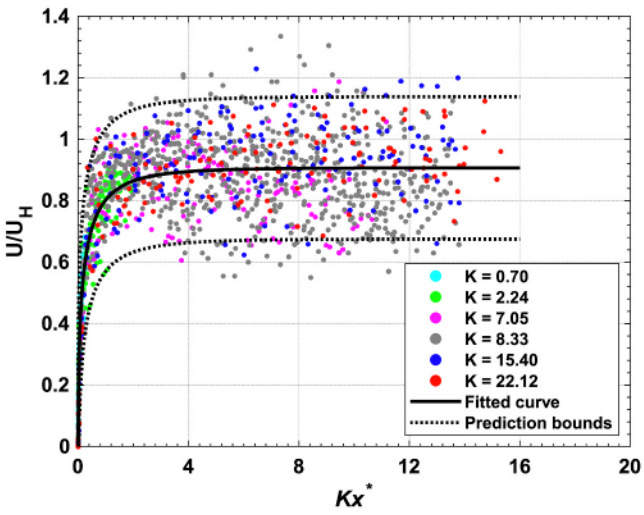

(a)

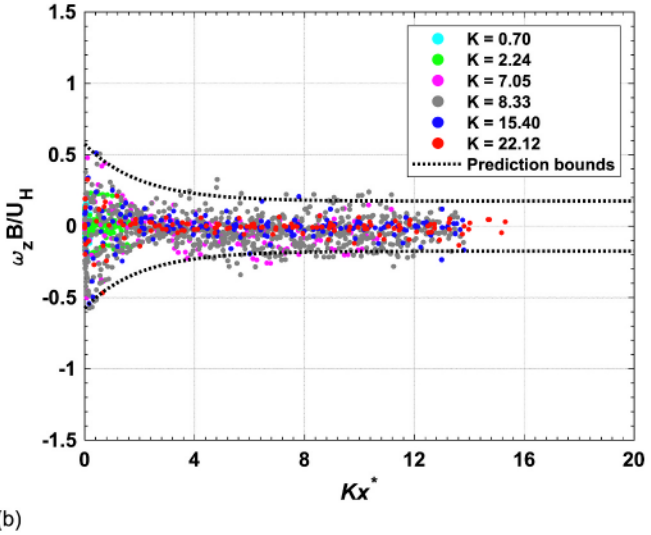

(b)

Fig. 19. (a) Normalized horizontal velocity versus non-dimensional horizontal travel distance, and (b) normalized angular velocity versus non-dimensional horizontal travel distance obtained for plate-type debris objects.

- Based on a detailed comparison of debris flight trajectories in the uniform and ABL winds, significant variations were noted, in terms of translational and angular displacements obtained for the debris. At several pitch angles, the plate was found to travel farther in the ABL wind than in the uniform wind. This was explained by the significant lift experienced by the plate, especially if the pitch angle was 0°. The provided observations reflected how a transition from the simulations with a uniform wind to those with an ABL wind, as presented for the first time in the current study, can improve the accuracy of predictions.
- From the simulation results, the debris flight trajectories were found to be strongly dependent on the initial pitch angle. The plates with an initial pitch angle less than 90° first moved upward due to the positive lift, while the plates with an initial pitch angle higher than 90° moved downward due to the negative lift. As for the yaw angle, the conducted simulations covered a range of yaw angles from 0° to 75°. In particular, it was noted that the plates experience significant lateral movements if the initial yaw angle is increased. Several plates were also observed to traverse their flight paths. To estimate the kinetic impact energy, the translational and angular velocity components were systematically recorded as a function of time. For several plates, the horizontal velocity was observed to exceed the mean wind velocity, while the vertical and angular velocities consistently reduced with the increase of flight time.
- The CFD-RBD simulations were further extended to study the effects of different plate characteristics, mean wind velocities, and release heights. From this holistic investigation, the horizontal distance traveled by the plate was found to increase with the increase in the Tachikawa number. The lift forces experienced by the plates reduced with decreasing the plate's surface area and increased with increasing the plate's mass. The plates with a high Tachikawa number, in particular, showed notable deviations from a linear flight trajectory. This was further confirmed through the study of different plate types and mean wind velocities.
- To estimate the likelihood and intensity of impact, this study proposed three closed-form equations to predict the horizontal distance traveled by the plate-type debris objects, as well as the linear and angular velocities associated with them. This was presented along with upper and lower bounds, providing the flexibility required for the vulnerability assessment of building envelopes under the windborne debris hazard, depending on the level of risk that can be tolerated.

The debris flight trajectories reported in the current study covered various pitch and yaw angles, plate characteristics, mean wind velocities, and release heights. While the wide ranges considered for the key contributing factors successfully captured the variations commonly observed in debris flight trajectories, a separate study for uncertainty quantification is recommended. It must also be noted that the simulations performed in this study utilized neutral, horizontally-homogenous ABL winds. This led to obtaining mean flight trajectories. While the outcome of the current study advanced the state of the knowledge in this study domain through making a transition from uniform to ABL wind simulations, the investigation of variability due to atmospheric turbulence fluctuations fell beyond the scope of the current study. Thus, future research is recommended to study debris flight in a thermally neutral boundary layer that can simulate the turbulence with full details. For this purpose, the large eddy simulation (LES) approach can be employed and the predictive models can be further refined. This will build on the wealth of results and findings from the current study to further advance the hazard models related to windborne debris.

CRediT authorship contribution statement

Dikshant Saini: Methodology, Software, Validation, Investigation, Writing – original draft. **Behrouz Shafei:** Conceptualization, Methodology, Investigation, Writing – review & editing, Supervision, Funding acquisition.

Declaration of competing interest

The authors declare that they have no known competing financial interests or personal relationships that could have appeared to influence the work reported in this paper.

Acknowledgement

The research study, results of which reported in this manuscript, was partially sponsored by the National Science Foundation (NSF) under Grants No. 1826356 and 1827774. The authors would like to acknowledge and thank the sponsor for this support. Opinions, findings, and conclusions expressed in this manuscript are of the authors and do not necessarily reflect those of the NSF.

References

Andersen, A., Pesavento, U., Wang, Z.J., 2005. Unsteady aerodynamics of fluttering and tumbling plates. J. Fluid Mech. 541, 65–90.
Baker, C.J., 2007. The debris flight equations. J. Wind Eng. Ind. Aerod. 95 (5), 329–353.
Baker, C.J., Sterling, M., 2017. Modelling wind fields and debris flight in tornadoes. J. Wind Eng. Ind. Aerod. 168, 312–321.
Beason, W.L., Meyers, G.E., James, R.W., 1984. Hurricane related window glass damage in Houston. J. Struct. Eng. 110 (12), 2843–2857.
Brown, J., Bogdanoff, D., Yates, L., Wilder, M., Murman, S., 2006. Complex-trajectory aerodynamics data for code validation from a new free-flight facility. 44th AIAA Aerospace Sciences Meeting and Exhibit 662, 1–15, 2006.
Costello, M., Gatto, S., Sahu, J., 2007. Using Computational Fluid Dynamics-Rigid Body Dynamic (CFD-RBD) Results to Generate Aerodynamic Models for Projectile Flight Simulation. " *Army Research Laboratory*. ARL-TR-4270.
ESDU, 1970. Fluid Forces and Moments on Flat Plates, 70015. Engineering Science Data Unit, London, UK.
ESDU, 1990. Characteristics of Atmospheric Turbulence Near the Ground. Part II, Single Point Data for Strong Winds (Neutral Atmosphere), 85020. Engineering Sciences Data Unit, London, UK.
FEMA, 2006. Hurricane Katrina in the Gulf Coast Building Performance Observations, Recommendations, and Technical Guidance, vol. 549. " *Federal Emergency Management Agency*, FEMA, Washington, DC.
FEMA, 2011. Coastal Construction Manual: Principles and Practices of Planning, Siting, Designing, Constructing, and Maintaining Residential Buildings in Coastal Areas. " *Federal Emergency Management Agency*, FEMA P-55, Washington, DC.
Grayson, M., Pang, W., Schiff, S., 2012. Three-dimensional probabilistic wind-borne debris trajectory model for building envelope impact risk assessment. J. Wind Eng. Ind. Aerod. 102, 22–35.
Holmes, J.D., 2004. Trajectories of spheres in strong winds with application to windborne debris. J. Wind Eng. Ind. Aerod. 92 (1), 9–22.
Holmes, J.D., Letchford, C.W., Lin, N., 2006. "Investigations of plate-type windborne debris—Part II: computed trajectories. J. Wind Eng. Ind. Aerod. 94 (1), 21–39.
Jin, C., Xu, K., 2008. Numerical study of the unsteady aerodynamics of freely falling plates. Commun. Comput. Phys. 3 (4), 834–851.
Kakimpa, B., 2012. The Numerical Simulation of Plate-type Windborne Debris Flight. " Doctoral Dissertation, University of Nottingham, England.
Kakimpa, B., Hargreaves, D.M., Owen, J.S., Martinez-Vazquez, P., Baker, C.J., Sterling, M., Quinn, A.D., 2010. CFD modelling of free-flight and auto-rotation of plate type debris. Wind Struct. 13 (2), 169–189.
Kakimpa, B., Hargreaves, D.M., Owen, J.S., 2012a. An investigation of plate-type windborne debris flight using coupled CFD–RBD models. Part I: model development and validation. J. Wind Eng. Ind. Aerod. 111, 95–103.
Kakimpa, B., Hargreaves, D.M., Owen, J.S., 2012b. An investigation of plate-type windborne debris flight using coupled CFD–RBD models. Part II: free and constrained flight. J. Wind Eng. Ind. Aerod. 111, 104–116.
Kordi, B., Kopp, G.A., 2011. Effects of initial conditions on the flight of windborne plate debris. J. Wind Eng. Ind. Aerod. 99 (5), 601–614.
Kordi, B., Traczuk, G., Kopp, G.A., 2010. Effects of wind direction on the flight trajectories of roof sheathing panels under high winds. Wind Struct. 13 (2), 145–167.
Kulkarni, A., Shafei, B., 2021. Investigation of windborne debris impact on ultra-high performance concrete wall panels. J. Build. Eng. 103004, 1–16. https://doi.org/10.1016/j.jobe.2021.103004.
Lee, A.J.H., 1974. A general study of tornado-generated missiles. Nucl. Eng. Des. 30 (3), 418–433.
Lin, N., Letchford, C., Holmes, J., 2006. Investigation of plate-type windborne debris. Part I. Experiments in wind tunnel and full scale. J. Wind Eng. Ind. Aerod. 94 (2), 51–76.
Lin, N., Holmes, J.D., Letchford, C.W., 2007. Trajectories of wind-borne debris in horizontal winds and applications to impact testing. J. Struct. Eng. 133 (2), 274–282.
Martinez-Vazquez, P., Baker, C.J., Sterling, M., Quinn, A., Richards, P.J., 2010. Aerodynamic forces on fixed and rotating plates. Wind Struct. 13 (2), 127–144.

Minor, J.E., 1994. Windborne debris and the building envelope. J. Wind Eng. Ind. Aerod. 53 (1–2), 207–227.
Murakami, S., Mochida, A., Hibi, K., 1987. Three-dimensional numerical simulation of air flow around a cubic model by means of large eddy simulation. J. Wind Eng. Ind. Aerod. 25 (3), 291–305.
Murman, S., Aftosmis, M., Rogers, S., 2005. Characterization of space shuttle ascent debris using CFD methods. 43rd AIAA Aerospace Sciences Meeting and Exhibit 1223, 1–20, 2005.
Noda, M., Nagao, F., 2010. Simulation of 6DOF Motion of 3D Flying Debris. " *5th International Symposium on Computational Wind Engineering*, Chapel Hill, NC.
Oliver, C., Hanson, C., 1992. Failure of residential building envelopes as a result of hurricane andrew in dade county, Florida. In: Hurricanes of 1992: Lessons Learned and Implications for the Future. American Society of Civil Engineers, pp. 396–508.
Redmann, G.H., Radbill, J.R., Marte, J.E., Dergarabedian, P., Fendell, F.E., 1978. Wind Field and Trajectory Models for Tornado-Propelled Objects. " *Jet Propulsion Laboratory*, Pasadena, CA.
Reed, J.W., 1970. "Window Damage Study of the Lubbock tornado." Sandia National Laboratories. Report No. SC-TM-70-535, Albuquerque, NM.
Richards, P.J., Hoxey, R.P., 1993. Appropriate boundary conditions for computational wind engineering models using the k-ε turbulence model. Computational Wind Engineering 46–47, 145–153.
Richards, P.J., Williams, N., Laing, B., McCarty, M., Pond, M., 2008. Numerical calculation of the three-dimensional motion of wind-borne debris. J. Wind Eng. Ind. Aerod. 96 (10), 2188–2202.
Saini, D., Shafei, B., 2020a. Performance of structural insulated panels with metal skins subjected to windborne debris impact. Journal of Composites Part B: Engineering 198, 1–12, 108163.
Saini, D., Shafei, B., 2020b. Damage assessment of wood frame shear walls subjected to lateral wind load and windborne debris impact. J. Wind Eng. Ind. Aerod. 198, 1–13, 104091.
Saini, D., Shafei, B., 2021. Design optimization of double-layered structural insulated panels for windborne debris hazard. Journal of Composites Part B: Engineering 216, 1–13, 108806.
Simiu, E., Scanlan, R.H., 1978. Wind Effects on Structures: an Introduction to Wind Engineering. " Wiley.
Stephenson, A.E., Sliter, G.E., Burdette, E.G., 1978. Full-scale tornado-missile impact tests. Nucl. Eng. Des. 46 (1), 123–143.
Tachikawa, M., 1983. Trajectories of flat plates in uniform flow with application to wind-generated missiles. J. Wind Eng. Ind. Aerod. 14 (1–3), 443–453.
Tachikawa, M., 1988. A method for estimating the distribution range of trajectories of wind-borne missiles. J. Wind Eng. Ind. Aerod. 29 (1–3), 175–184.
Twisdale, L.A., Dunn, W.L., Davis, T.L., 1979. Tornado missile transport analysis. Nucl. Eng. Des. 51 (2), 295–308.
Uchibori, K., Tamura, T., 2019. LES study on aerodynamics of auto-rotating square flat plate by IBM and SAMR. J. Fluid Struct. 89, 108–122.
Visscher, B.T., Kopp, G.A., 2007. Trajectories of roof sheathing panels under high winds. J. Wind Eng. Ind. Aerod. 95 (8), 697–713.
Wills, J.A.B., Lee, B.E., Wyatt, T.A., 2002. A model of wind-borne debris damage. J. Wind Eng. Ind. Aerod. 90 (4), 555–565.